



ELSEVIER

Available online at www.sciencedirect.com**ScienceDirect**journal homepage: www.intl.elsevierhealth.com/journals/dema

Towards quantitative analysis of enamel erosion by focused ion beam tomography

Nancie Cougot^{a,b,*}, Thierry Douillard^c, Florent Dalmas^c, Nelly Pradelle^{a,b}, Rémy Gauthier^d, Clarisse Sanon^c, Brigitte Grosgogeat^e, Pierre Colon^{a,b}, Jérôme Chevalier^c

^a Univ. Paris Diderot, AP-HP, Hôpital Rothschild, UFR Odontologie, Paris, France

^b Univ. Lyon, Université Claude Bernard Lyon 1, Laboratoire des Multimatériaux et Interfaces, UMR CNRS 5615, 69008 Lyon, France

^c Univ. Lyon, INSA-LYON, MATEIS, UMR CNRS 5510, F69621 Villeurbanne, France

^d Univ. Lyon, Université Claude Bernard Lyon 1, IFSTTAR, LBMC UMR_T9406, F69622 Lyon, France

^e Univ. Lyon, Université Claude Bernard Lyon 1, UFR d'Odontologie, Service de Traitements et de Consultations Dentaires, Hospices Civils de Lyon, Laboratoire des Multimatériaux et Interfaces, UMR CNRS 5615, 69008 Lyon, France

ARTICLE INFO

Article history:

Received 27 March 2018

Received in revised form

30 July 2018

Accepted 27 August 2018

Available online xxx

Keywords:

Erosion

Tooth wear

Scanning electron microscopy

Demineralization

Ultrastructure

ABSTRACT

Objectives. The purpose of this work is a proof of concept to introduce a new quantitative 3D-analysis of dental erosion obtained by focused ion beam (FIB) tomography associated with silver nitrate penetration into porosities in etched enamel.

Methods. One sample selected was sound enamel after removal of the aprismatic surface. The other was studied after applying an additional attack with orthophosphoric acid. Both surfaces were infiltrated with silver nitrate via immersion. After dehydration, samples were observed in a dual column FIB/SEM station. Serial FIB sectioning was conducted with a current of 3 nA at 30 keV and an increment step of 20 nm for the healthy enamel and of 40 nm for the etched one. 3D analysis was performed with Fiji software and BoneJ plugin and several parameters were obtained to characterize the tissue: non-mineralized phase content (NMP), connected porosity fraction (CPF) and degree of anisotropy (DA) of the NMP. **Results.** Healthy enamel showed an NMP content of 0.5 vol.%, with a bimodal distribution of non-mineralized regions, inside the prisms and between the prisms. No silver penetration was noticed in the healthy enamel, demonstrating the absence of open porosity. In contrast, silver nitrate penetration after acidic exposure was observed, up to a depth of 12 µm, which allowed the calculation of an interconnected porosity volume fraction (CPF) of 3.1 vol.%, mostly between the prisms. Values for DA of 0.56 for sound enamel and 0.81 for acid-etched surface were determined, highlighting a higher degree of anisotropy in the latter.

* Corresponding author at: UFR d'odontologie – Université paris-diderot, 5 rue Garancière 75006 Paris, France.

E-mail address: dr.cougot.nancie@gmail.com (N. Cougot).

<https://doi.org/10.1016/j.dental.2018.08.304>

0109-5641/© 2018 The Academy of Dental Materials. Published by Elsevier Inc. All rights reserved.

Significance. Quantitative analysis of FIB tomography using NMP, CPF and DA should contribute to a better understanding and follow up of dental erosion, correlation between erosion and attrition or abrasion process, and the ability to develop enamel remineralization procedures.

© 2018 The Academy of Dental Materials. Published by Elsevier Inc. All rights reserved.

1. Introduction

The first studies concerning human dental enamel erosion were focused on dental adhesion and etching patterns after phosphoric acid attack [1]. Today, there is also a need to follow and understand the features of dental erosion as far as nutrition is concerned, since acidic beverages or pathological diseases may lead to a fast and deep degradation [2]. The dental enamel histological structure after acid exposure can be described by the three well-known patterns classified as type 1 (intraprismatic), type 2 (interprismatic), and type 3 (combined). Therefore, the aim of the first studies was a better understanding of the acid dissolution of hydroxyapatite in relation to the c axis prisms orientation and to the crystal size. It is known that mineral is dissolved from the surface causing a roughening of the surface, but the depth of dissolution in the partly demineralized zone remains unclear [3,4]. Many surface characterization techniques have been used to assess human enamel erosion patterns. Scanning electron microscopy (SEM), surface profilometry, confocal laser scanning microscopy, and atomic force microscopy have all been reported [5–7], but fail to fully characterize the extent and degree of demineralization below the surface.

Among tomographic methods, focused ion beam (FIB) tomography, based on the use of a focused ion beam in a SEM, appears to provide quite exciting opportunities, particularly in life science. In this field, researchers suggest a quiet revolution for nanoscale cellular imaging [8]. Indeed, FIB tomography recently revealed aspects of HIV biology that could not be captured by 2D imaging [9]. For example, large volumes of Drosophila brain have been reconstructed for connectome tracing [10]. The ultrastructure of a diatom has been explored as a whole in the framework of a diatom domestication project for biofuel production [11]. FIB tomography is of course involved in correlative tomography purpose both on biological samples and in material science [12–14]. Moreover, methodology improvements are under development [15] and new areas are starting to open with the emergence of new FIB sources [16,17] or with the emerging use of cryo-configuration applied to biological and “soft” polymeric materials [18,19].

In the field of energy materials, the spatial distribution, volume fraction, size, shape, specific surface area, connectivity and tortuosity of pores and solid phase components are key parameters for the improvement of energy capacity, power density and cycle life of batteries. Sophisticated FIB tomography analyses have been set up to provides such advanced quantitative data [20,21].

FIB/SEM is an ion column that delivers a focused ion beam, coupled to a SEM, first of all allowing to machine matter with

nanometric precision and under electron images control. This is actually a multi-function facility. Unlike electrons, the higher-mass ions have the ability to dislodge neutral and charged particles (atoms, molecules) from a sample surface in a process called sputtering or milling. For a focused ion beam, scanning coils allow the ion beam to pattern or section many materials with a nanometric resolution. It is also possible to transform this natural mechanism of ion milling by a deposition process. Indeed, most FIBs are now usually equipped with a gas injection system containing one or several reservoirs of solid or liquid precursor material to deposit material with a level of precision close to FIB milling (Platinum, tungsten or carbon deposition are commonly performed) [22]. Nanorobotic plateforms are also often integrated inside dual column FIB/SEM instruments [23] as analytical tools like electron backscatter diffraction (EBSD) or energy dispersive X-ray (EDX).

This opens the door to numerous applications including tomography. Most of these various potentials have been already well exploited in the field of dental research, oral implant or materials for restorative dentistry.

FIB cross-section was used to observe subsurface damage induced by wear of human enamel in different acidic environments [24,25]. Both studies concluded that a higher loss of enamel in acidic environment was associated with a wear mechanism. They also noticed a mechanism of “delamination” when wear occur in a neutral solution (such as distilled water) whilst “shaving” process was identified in an acidic environment. FIB cross-section was also used to investigate indentation profiles and especially fracture scenarios after indentation of coating systems (used to improve the aesthetical appearance of Ti-based dental implants) to select refined fracture toughness assessment models [26].

The usefulness of the focused ion beam for the preparation of transmission electron microscopy samples from a specific site has been demonstrated in studies on remineralization of enamel in human saliva [27], for the characterization of resin-dentin interface [28], dentin-enamel interface [29], and resin-enamel interface [30] as well as the evaluation of repair potential for chitosan hydrogel on enamel [31].

Even more startling, a new class of methods for residual stress evaluation has been proposed, based on the use of FIB machining providing local stress relaxation, which is directly measured by digital image correlation (DIC). Thus, it was possible to analyze the residual stress distribution for a veneering ceramic on a zirconia framework and to correlate stress field with indentation fracture toughness [32]. Quantification of residual stress in the vicinity of the dentin enamel junction which exhibits remarkable strength and durability

has also been performed [33]. The results are likely to inspire biomimetic materials engineering.

FIB milling is also useful for specimen shaping. Indeed, it was implemented to produce micro-cantilevers within the dentin-enamel junction and with respect to prism orientation for further bending test. Such experience demonstrated an important anisotropy commensurate with the microstructure of enamel which was not measurable using nanoindentation on bulk samples [34]. Micropillars with micron-scale diameters have also been milled by FIB and tested in compression with a nanoindenter to study the lower mechanical properties of degraded layer in aged Yttria-doped Tetragonal Polycrystalline Zirconia [35].

FIB tomography has been performed on zirconia grades used for restorative dentistry and oral implants. Structural modification and sub-surface microcracks were highlighted within a veneer-zirconia interface using this 3D-analysis tool [36]. Such a tomographic technique was also used to understand the morphology of cracks beneath indentation marks in feldspathic dental porcelain on zirconia [37]. In addition, microcracking due to aging has been studied on laboratory samples in zirconia, alumina-toughened zirconia (ATZ) and zirconia-toughened alumina (ZTA) [38,39]. FIB tomography also served in a study on the effect of hydrothermal aging on one-piece ceramic oral implants with a porous surface [40]. Systematically in this instance, this technique proved essential to obtain reliable information on the durability of zirconia.

For human dental tissue, FIB Tomography experiments have been performed on dentin structure. In these studies, the viability of 3D characterization of dentin tubule structure has been demonstrated [41,42]. Another study showed that a reliable evaluation of nano-leakage distribution at adhesive-dentin interfaces requires tomography and that TEM 2D-image projections are unable to provide reliable quantitative data for such complex structures [43].

In attempting to build on the 3D images of dental tissue previously published, the aim of our study was to use FIB technology to quantify the porous volume and the interconnection of porosities in the eroded enamel subsurface. Furthermore, it is proposed that the anisotropic degree calculation, as previously described for bone [44–46] could be used for a better understanding of the acid attack influence on the structure of dental enamel. The anisotropic degree values, before and after acid attack, could be helpful to study the diffusion potential of different materials into etched enamel.

2. Materials and methods

2.1. Human enamel samples

Human third molars, requiring removal for orthodontic reasons were gathered from individuals following signed consent. Two extracted third molars stored in a 1% chloramine solution at 4 °C for up to one month were used for this study. Before experimentation, tissue remnants on the roots were removed by hand scaling. The teeth were immersed in an ultrasonic bath with distilled water for five minutes and kept in distilled water at 37 °C. Using a diamond saw (Accutome® Struers, Copenhagen, Denmark) under water, the radicular

portion was sectioned. Afterwards, with a diamond drill, all the dentin was removed to conserve only enamel. The specimens obtained were embedded in epoxy resin with the buccal side above and polished with abrasive discs to remove aprismatic enamel. Samples were polished with diamond pastes down to a 1 µm particle size. The enamel surface on one sample was demineralized with orthophosphoric acid at 37% (30 s immersion) and water rinsed, while healthy enamel was preserved on the other. Both samples were immersed in a 50 weight % silver nitrate aqueous solution for 2 h in total darkness. Following subsequent retrieval, the samples were placed in distilled water and exposed to fluorescent light for 12 h. Specimens were immersed for 2 h in photodeveloping solution (Kodak SA) and thoroughly water-rinsed. They were then dehydrated in ascending grades of ethanol (25% for 20 min, 50% for 20 min, 75% for 20 min and 100% for 20 min). After the final ethanol step, they were dried in HMDS (Hexa Methyl Di Silizane) for 10 min and placed on a filter paper inside a covered glass vial at room temperature. At each time point, the analysed sample was glued with a silver paint onto an aluminium stub. Finally, to make the surface electrically conductive, the samples were coated with a 30 nm carbon layer using thermal evaporation (EM SCD500, Leica Microsystems GmbH, Germany).

2.2. 3D focused ion beam tomography

Both specimens (healthy and etched human tooth enamel) were studied by FIB tomography.

Serial FIB/SEM imaging was performed using a FIB/SEM workstation (NVision 40; Carl Zeiss Microscopy GmbH, Oberkochen, Germany) combining a SIINT zeta FIB column (Seiko Instruments Inc., NanoTechnology, Japan) with a Gemini I SEM column. The NVision 40 platform was also equipped with a multi-nozzle SIINT gas injection system. The angle between the FIB and SEM columns was 54°.

The principle of FIB tomography is based on stacking 2D images, obtained by performing serial FIB sectioning and SEM imaging, to reconstruct the microstructure in three dimensions. Acquisitions of such stacks were done by alternated imaging and milling.

Before running the acquisition, a carbon layer was deposited on the volume of interest by *in situ* ion beam induced deposition. This smoothed out the surface roughness during slicing, to deliver sharp upper edges and to minimize curtaining artefacts (i.e. vertical stripes on the cross-section induced by ion milling, partly due to the sensitivity of the sputtering yield with respect to the angle of incidence and to phases). Then, several reference lines were imprinted into the carbon layer and fulfilled *in situ* with tungsten for reliable post-stack alignment purposes (Fig. 1). Indeed, the typical acquisition time for FIB tomography is more than ten hours. During such a long data run, drifts in the x-y plane occur. Sources of drift are numerous: electro-static charge effects, mechanical instability, electromagnetic perturbations, thermal variation, stability of the whole microscope and the electron-optical system. Image processing algorithms allow alignment of stack of image slices with cross-correlation measurements. With such methodology, each slice is used as the template with respect to which the next slice being aligned, so

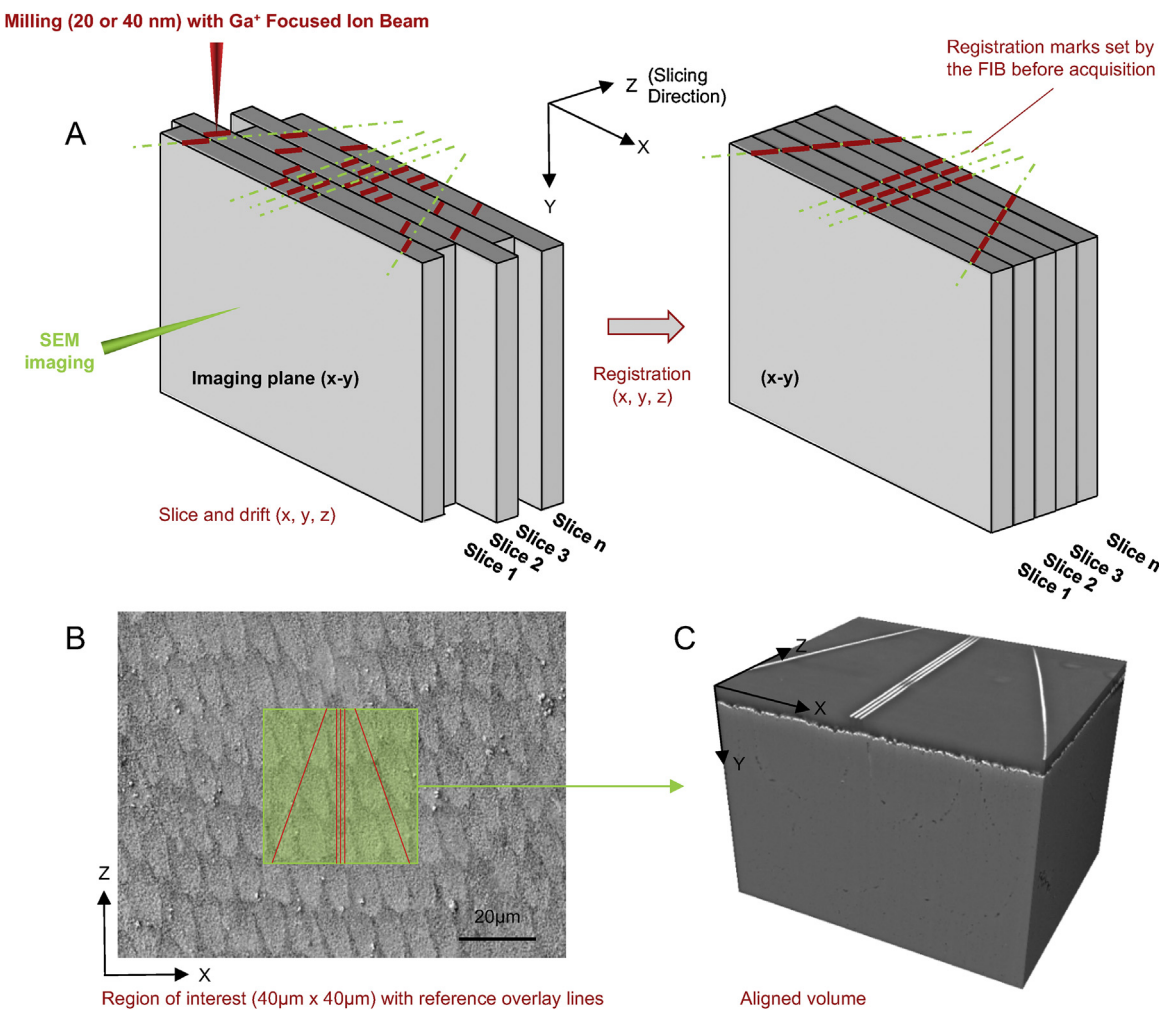


Fig. 1 – Schematics of 3D focused ion beam tomography improved with a refined drift correction procedure. (A) Schematic illustration showing shifts in the x-y plane occurring between the individual slices during acquisition and the post-acquisition image registration based on reference marks. Such pattern of reference marks can be used to correct image drifts with a cross-correlation algorithm. This refined correction leads to a more reliable reconstruction of the volume. **(B)** Reference chevron pattern overlaid to a SEM image of a flat surface of enamel. These reference notches consist of imprinted electron beam induced tungsten deposition into an ion beam induced carbon coating of the volume of interest. **(C)** Example of an extracted registered volume of enamel.

that the alignment proceeds by propagation. But a registration using an image-to-image based correlation tends to align the dominant feature in straight lines. Paradoxically, use of such an algorithm may misalign rather than align. So, to overcome this issue and for precise 3D reconstruction, we used straight registration marks to remove small shifts between the individual images in the x-y plane (Fig. 1A–C). SEM imaging was done in secondary electron (SE) mode with an accelerating voltage of 1.5 keV and a classic Everhart–Thornley detector. Prior to serial sectioning, a trench was milled to a depth that freed up sufficient cross-sectional surface. This step was performed with a coarse ion beam current of 27 nA with an accelerating voltage of 30 keV. Then, serial FIB sectioning was done with a current of 3 nA at 30 keV and an increment step (i.e. z-spacing) of 20 nm for the healthy enamel sample and of 40 nm for the acid etched enamel sample. A cubic voxel size was used in both cases.

2.3. Image processing and analysis

Three-dimensional analysis using FIB tomography is essentially a two-step process. After acquisition of the raw data as described above, this dataset is taken offline for further processing and 3D visualization in order to reach 3D quantification (Fig. 2 A). All the image processing and analysis were performed with Fiji, an open source image processing package based on ImageJ software [47].

The typical workflow of image processing for FIB tomography includes inter-slice registration, data cropping, bleach correction (i.e. correction of the intensity decay which occurs with the progress of the acquisition), correction of the curtaining effect, shading correction of the background, segmentation/threshold operations, 3D visualization, 3D labeling and 3D quantification [48].

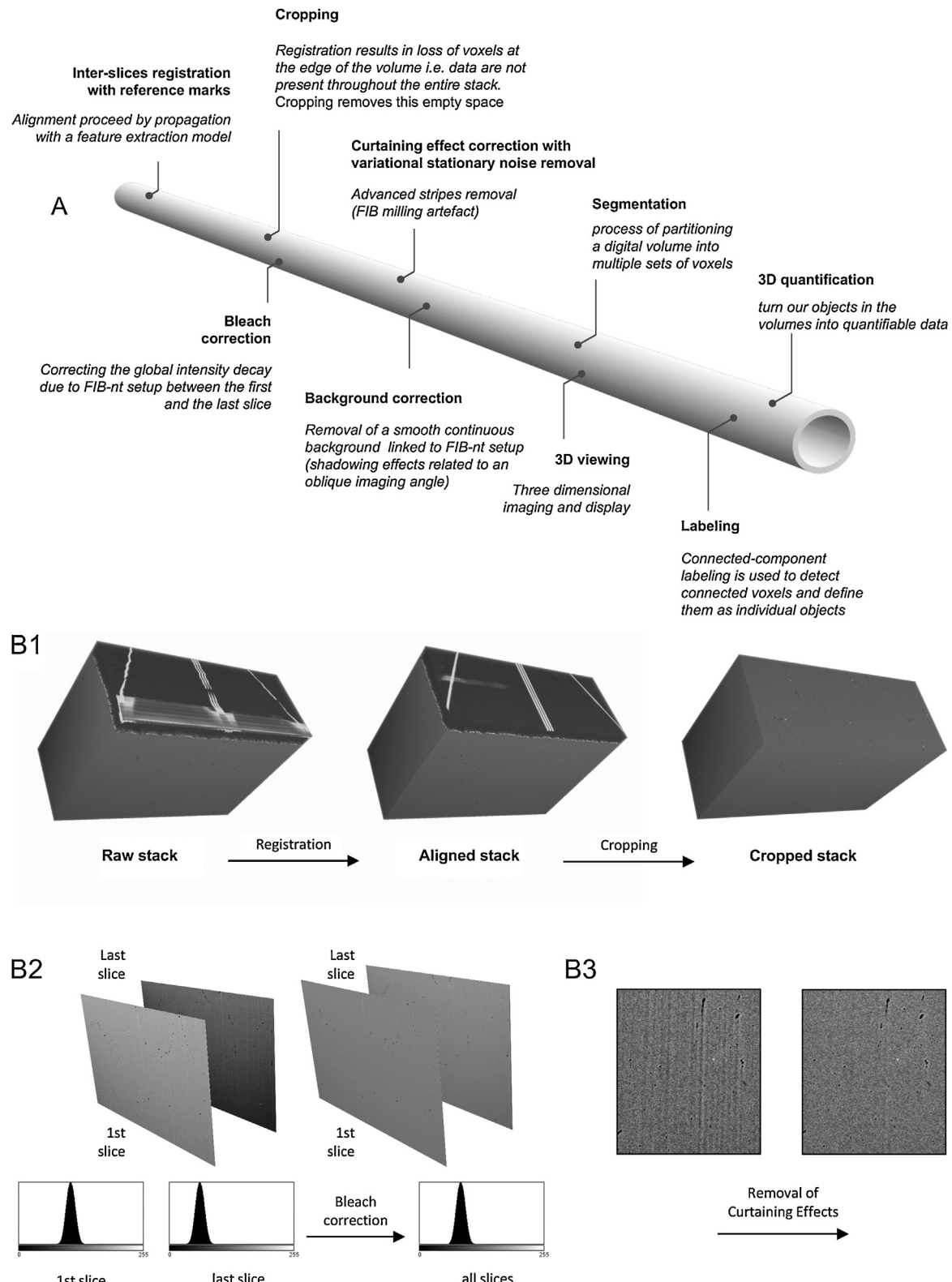
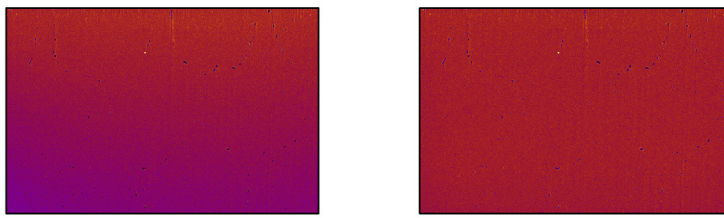


Fig. 2 – Detailed methodology to reach quantitative 3D focused ion beam tomography. (A) Typical image processing pipeline for quantitative 3D focused ion beam tomography. (B) Illustration of the successive steps of image processing (all processing algorithms are available in Fiji). (B1) Registration is usually the first step performed. Indeed, slice alignment has to be done to correct spatial drifts in x- and y-directions, which occur during FIB tomography processing. Registration results in a loss of voxels at the edge the volume i.e. data are not present throughout the entire stack. This is due to shifting of the images relative to one another. Since these data points are not useful, they are cropped away. (B2) Intensity variations occur along the entire stack. “Bleach correction” corrects for intensity fluctuations by normalizing the images of a stack to the same

B4



Background or shading correction



B5

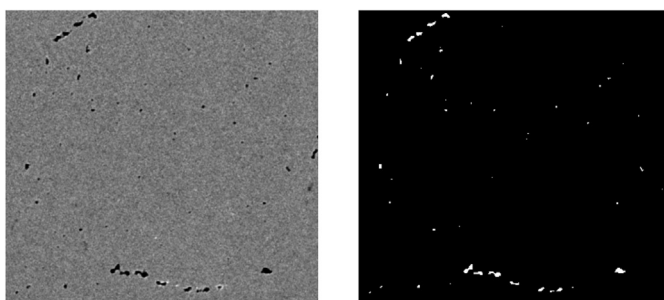
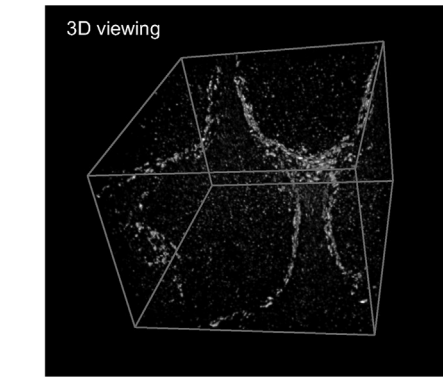


Image in grey level

Segmentation

Binarization of the Black
contrast in the n images
using contrast thresholding

3D viewing

Volume: $8,6 \times 6,5 \times 8 \mu\text{m}^3$
Voxel size target: $(20\text{nm})^3$

2 μm

Fig. 2 – (Continued)

Registration was achieved on the reference lines using the plugin MultiStakreg with a feature extraction model that accounted for translation. Reference chevron patterning also helped us to check that the slice thickness in the z-direction remained constant during the acquisition of the stack. The image contrast was then adjusted to correct its evolution upon ablation (z direction) and the shade effect (y direction) associated with the acquisition geometry. Finally, vertical stripes

(curtaining effect) on the SEM images, associated with the FIB milling, were removed using a variational algorithm [49]. Segmentation was then conducted for each slice using contrast thresholding, thus allowing for subsequent 3D viewing (Fig. 2B). Labeling (in this procedure, each cluster of connected voxels is numerically recognized as being an independent object i.e. each detected object is affected to a specific label) and quantification (size distribution of the segmented objects)

mean intensity (cf. grey levels histograms). (B3) An artefact induced by ion milling can affect the 3D reconstruction and is known as curtaining effect. Indeed, this undesirable effect results in the presence of vertical stripes on the face of interest. These stripes appear with light or dark contrast in SEM imaging. Their presence raises difficulties for subsequent image processing. These stripes can be assimilated to stationary noise (noise obtained by replicating and translating and elementary pattern). An advanced algorithm (namely Variational Stationary Noise Removal) was used to correct this kind of artefact. (B4) In FIB tomography, 2D images often suffer from illumination defects. Related to the oblique imaging angle and to the acquisition geometry, small brightness gradients appear in images (also called shading effect – cf. heat map of the background). Several ways can be explored to correct this: correction by Fast Fourier Transform (and band pass filter) or creation of a background from the original image and use of images operators. (B5) After filtering, the dataset is ready for visualization. But for further quantitative measurement, it is necessary to highlight certain features in the images, throughout the entire stack, in segmentation operations. This allows, for instance, the display of only certain inclusions in a bulk, thereby highlighting only the interesting or relevant parts of the data. Volume segmentation can be carried out by choosing suitable gray levels for thresholding. Here, a typical secondary electron SEM image of an acid-etched enamel infiltrated with silver nitrate aqueous solution (organic phase or pores appear dark and silver-nitrate particles are bright) and the corresponding segmentation are shown.

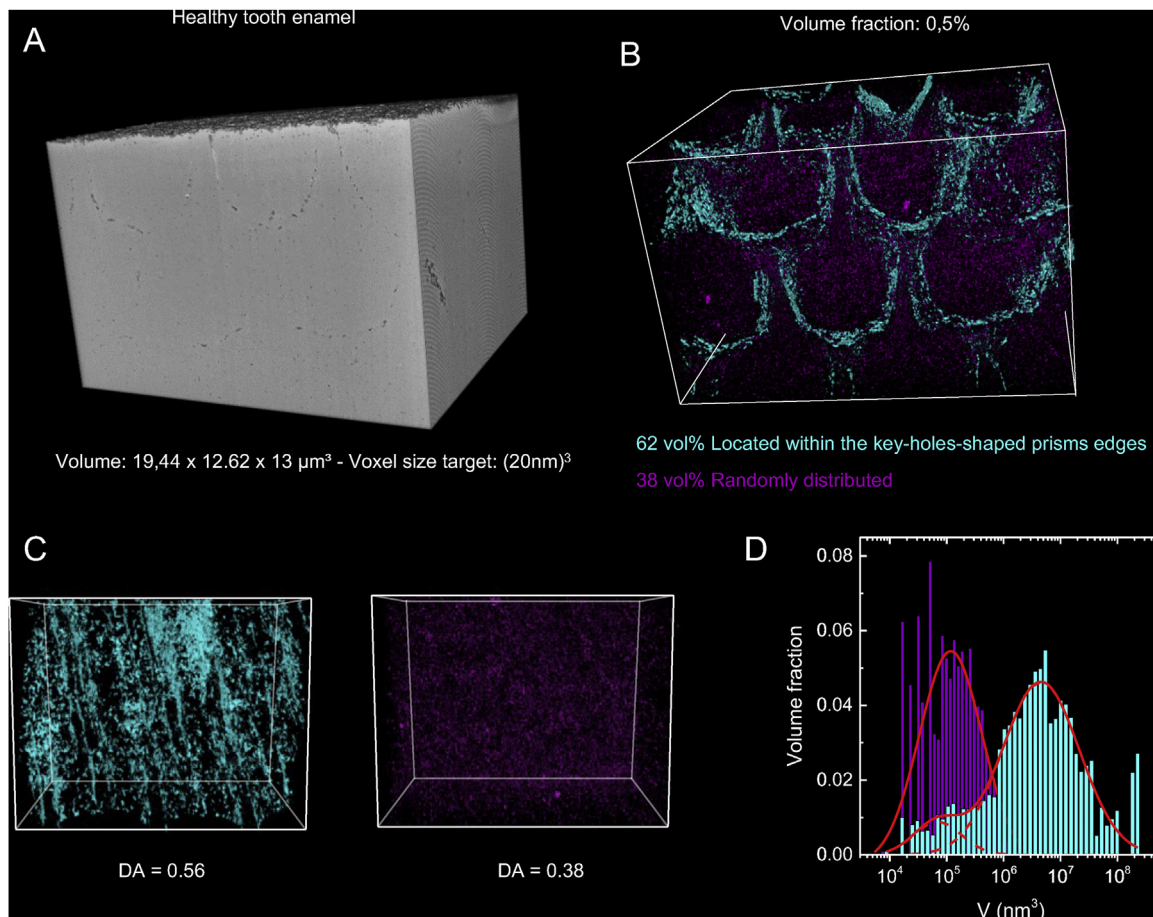


Fig. 3 – Healthy tooth enamel analysis. (A) Reconstructed volume, highlighting the absence of silver nitrate penetration after infiltration. (B) 3D Viewing of the distribution of the dark contrasts along the C-axis direction i.e. enameles rods. Part of black contrasts clearly draw the outline of the prisms (colored in cyan) while another population of black contrast is randomly distributed in the volume i.e. is located inside the prisms (colored in Magenta). (C) Separation of two contrast classes according to their location and 3D viewing in a random direction. Note that the phases defining the prisms are obviously larger in size. (D) Volume distribution of both types of black objects (deconvolution with Gaussian functions are shown in red lines).

were performed with the plugin Object Counter 3D [50]. Further analysis of the anisotropy of the volume was then done by computing the degree of anisotropy, (DA) using the Bone plugin [51]. This plugin, originally created for bones analysis, uses the mean intercept length (MIL) method extended to 3D for determining anisotropy [52] and provides in the present work a quantification of how highly oriented the objects are within a volume. The DA value ranges between 0 for isotropic to 1 for fully anisotropic structures.

3. Results

Fig. 3A shows the acquired volume for healthy enamel. No penetration of silver nitrate within the enamel is observed (otherwise a bright contrast would have been visible). This suggests that the observed dark phases in the volume do not correspond to open porosities but can be correlated to the protein and water rich phase. In this paper, we will use the term “non mineralized phase” (NMP) to describe this area. A

selective segmentation of these dark contrast highlights two types of objects dispersed either around prisms (at the prism sheath), or randomly in the volume (Fig. 3B). An overall volume fraction of 0.5 vol.% is found for this dark phase in the enamel volume. The size distribution of these objects extracted from the volume is presented in Fig. 3D: Small objects, with an average volume, V_{av} , of about 10^5 nm^3 , are mainly dispersed inside the prisms (only a few are observed in Fig. 3D, for the bimodal size distribution of objects at the interface of the prisms), whereas larger ones ($V_{av} = 5 \cdot 10^6 \text{ nm}^3$) are located at the prism sheath, as shown by the second intense Gaussian peak fitted for the size distribution of objects at the interface in Fig. 3D. DA values of 0.56 and 0.38 were found for dispersions of dark objects around and inside prisms, respectively (Fig. 3C).

The 3D observation of the etched enamel demonstrates the silver nitrate penetration (white contrast) through pores, mainly located at the inter-prismatic areas (Fig. 4). Silver nitrate penetration is clearly observed up to a depth of 12 μm , demonstrating the network of porosities from the surface to the subsurface. A quantification of this effect is presented in

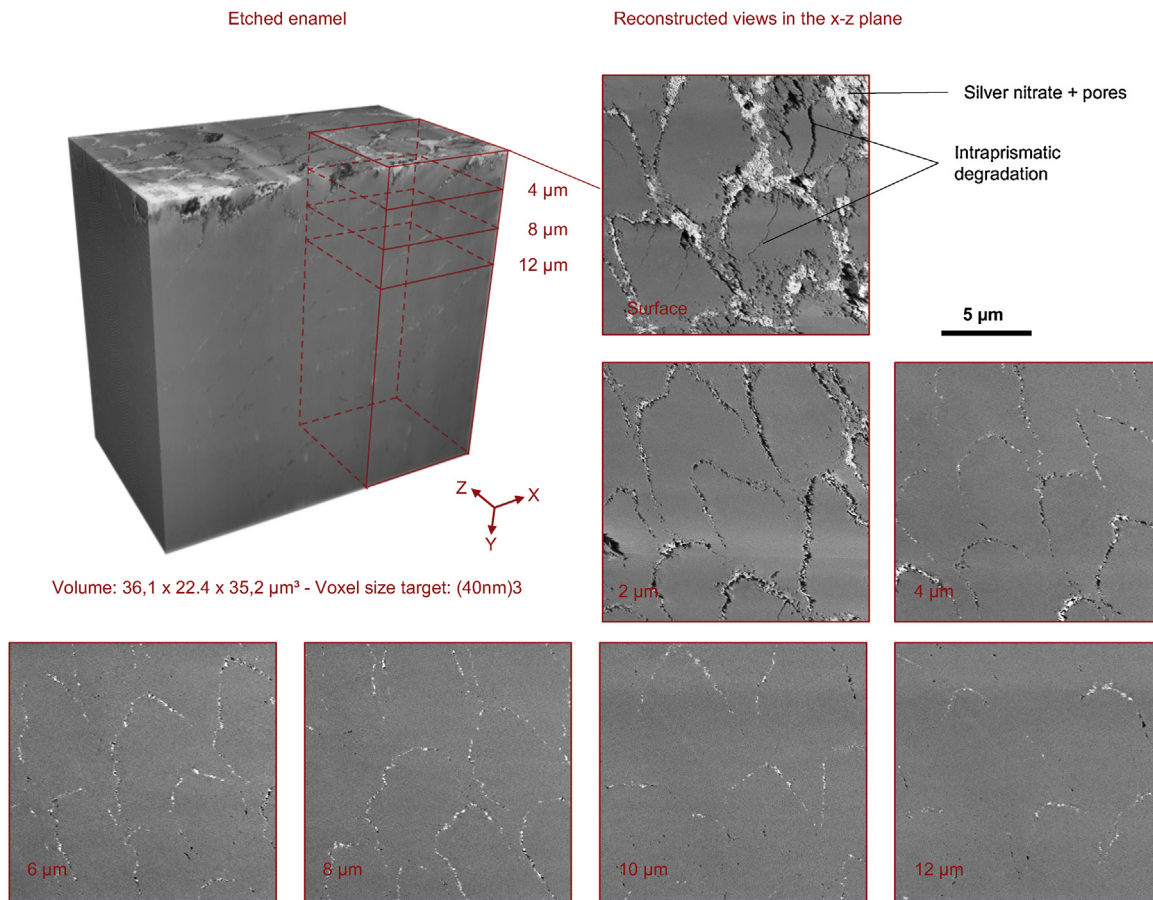


Fig. 4 – Virtual cross-section (x-z plane) through the stack for the chemically-etched and then infiltrated enamel (from the surface to 12 μm in depth with a step of 2 μm). This possibility to reconstruct these orthogonal views allows observation of both the penetration of silver nitrate at the boundary of the prisms and the decreasing amount with depth.

Fig. 5. A DA value of 0.81 is measured for the white objects with $V_{av} = 6.4 \cdot 10^6 \text{ nm}^3$, whereas the black object dispersion gives $DA = 0.27$ and $V_{av} = 1.6 \cdot 10^6 \text{ nm}^3$. A depth of penetration of about 12 μm (corresponding to the distance from the surface up to which 95% of the AgNO_3 has been detected in the volume) can be estimated (Fig. 5C). Then, by considering the same volume from the surface as the one analyzed in Fig. 3 for the healthy enamel, a total (AgNO_3 + black contrast) volume fraction of 3.1 vol.% is obtained in the etched enamel.

4. Discussion

4.1. Limits of the present work

Like other tomography techniques, a compromise has to be found in FIB/SEM between acquisition time (time for milling and 2D image recording), analyzed volume, resolution and size of the objects of interest. In fact, volume and resolution are linked together: for a constant image sampling (typically 1024×768 pixels), extending the volume implies increasing the voxel dimensions (i.e. decreasing the resolution). For the healthy human tooth enamel, our purpose was to have several prisms in the volume. To reach this goal with an image sampling of 1024×768 (i.e. a reasonable acquisition time around

30 s/slice), a pixel size of 20 nm led to a suitable area of $20.48 \mu\text{m} \times 15.36 \mu\text{m}$. For the etched human tooth enamel, the objective was rather to see how far silver nitrate had penetrated. To succeed, we had to multiply the area by four to reach $40.96 \mu\text{m} \times 30.72 \mu\text{m}$. This led us to have to increase the pixel size by a factor two and thus to go to a lower spatial resolution of 40 nm. It is worth to notice that such a decrease in resolution limits the detection of the black contrasts inside prisms, especially as several pixels in the 2D images are necessary to describe any object. On the other hand, such a resolution is not sufficient to track the connectivity of the silver particles beyond a few microns below the surface implying a slightly underestimated depth of penetration.

Only two samples were tested here, with the objective of assessing the feasibility and the relevance of such methodology in the quantification of the degradation of dental mineralized tissue in an erosion process. Due to the limited number of samples, the indicators obtained with the quantitative analysis (NMP content, DA, CPF) have no statistical values and the procedure should definitively be repeated on a large set of teeth, for different individuals to be used for a robust analysis of erosion process and its kinetics or its quantitative impact on dental enamel. However, it gives some clear and additional indications, as discussed below, on the process of dental erosion below the surface.

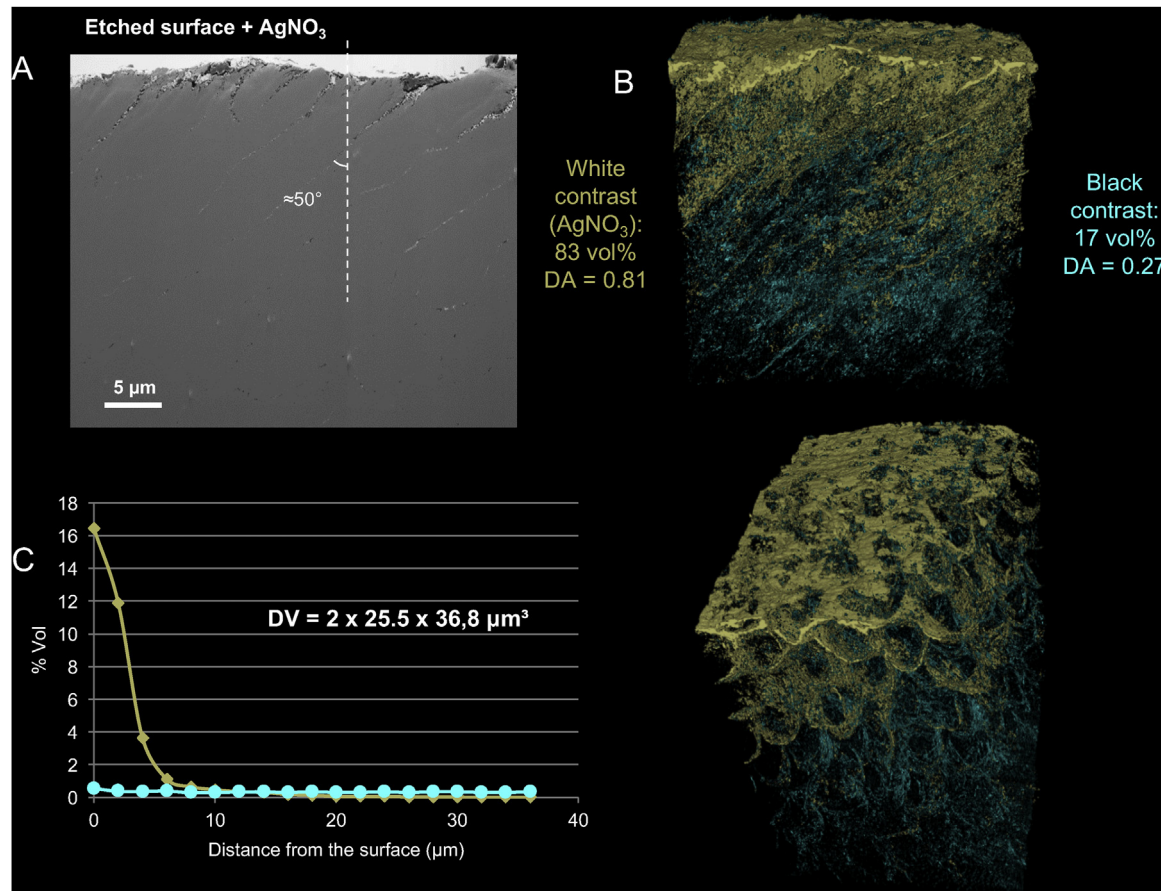


Fig. 5 – Quantitative evaluation of the infiltration of the silver nitrate after etching in 3D. (A) Slice in the x-y imaging plane showing the 50° orientation of the enamel rods compared to the normal of the surface. (B) 3D viewing of the diffusion of the silver nitrate, in the slicing direction on top and nearly in the c-axis in the bottom. (C) 3D Quantitative evaluation of the volume fraction of the silver nitrate particles and of the black contrasts assess by step of DV = $2 \times 25.5 \times 36.8 \mu\text{m}^3$.

4.2. New insights into dental erosion

The penetration process from the surface into the etched enamel is visualized by the AgNO_3 infiltration, which proves that the etching process creates connected porosities inside the enamel. These pores are preferentially created at the prisms sheath for the sample studied (class 2 of Silverstone). Even though the real loss of matter after etching is difficult to estimate, the volume fraction of porosities after etching is much higher than the one of NMP in the same representative volume for the healthy enamel; this suggests that the pores are not only created in the voids resulting from the degradation of the NMP but also result from a dissolution of the enamel. This hypothesis had been already formulated [53], and is quite clearly confirmed here. Furthermore, the dispersion of the pores within the enamel is highly anisotropic. The degradation process seems them to propagate according to one preferential direction, given by the inter-prismatic NMP alignment.

The quantitative 3D FIB methodology combined to silver nitrate penetration is a way to quantify not only the demineralized volume into the enamel structure but also the permeability of this volume. It could be of interest to optimize the penetration of adhesives, the ability to remineralize

by different products the eroded enamel or to explain the mechanism of dental erosion combined to attrition or abrasion phenomena [24,53–55].

The DA determination is a new information mainly used in the bone structures study. The 3D microstructural anisotropy quantification is known to approximate the macroscopic elastic orthotropy of trabecular bone [44]. Very recently, Musy et al. also proved, through finite element calculations, that volume fraction and DA also predict yield strength and failure onset of bones [45]. Then, by analogy with bone materials, the quantification of anisotropy and porosity proposed in the present study by mean of FIB tomography opens new perspectives as relevant input parameters for mechanical modeling and predictive approaches of enamel materials.

The enamel structure has been already demonstrated. FIB tomography associated to silver nitrate penetration is a methodology able to initiate the idea of “connected porosity network” and its evaluation by means of the connected porosity fraction (CPF). However, NMP is also highlighted by such FIB tomography as preferentially area for other acidic challenge.

Enamel is a hybrid material with prisms linked by a protein rich inter-prismatic area. After etching, this inter-prismatic area become porous explaining the mechanical properties

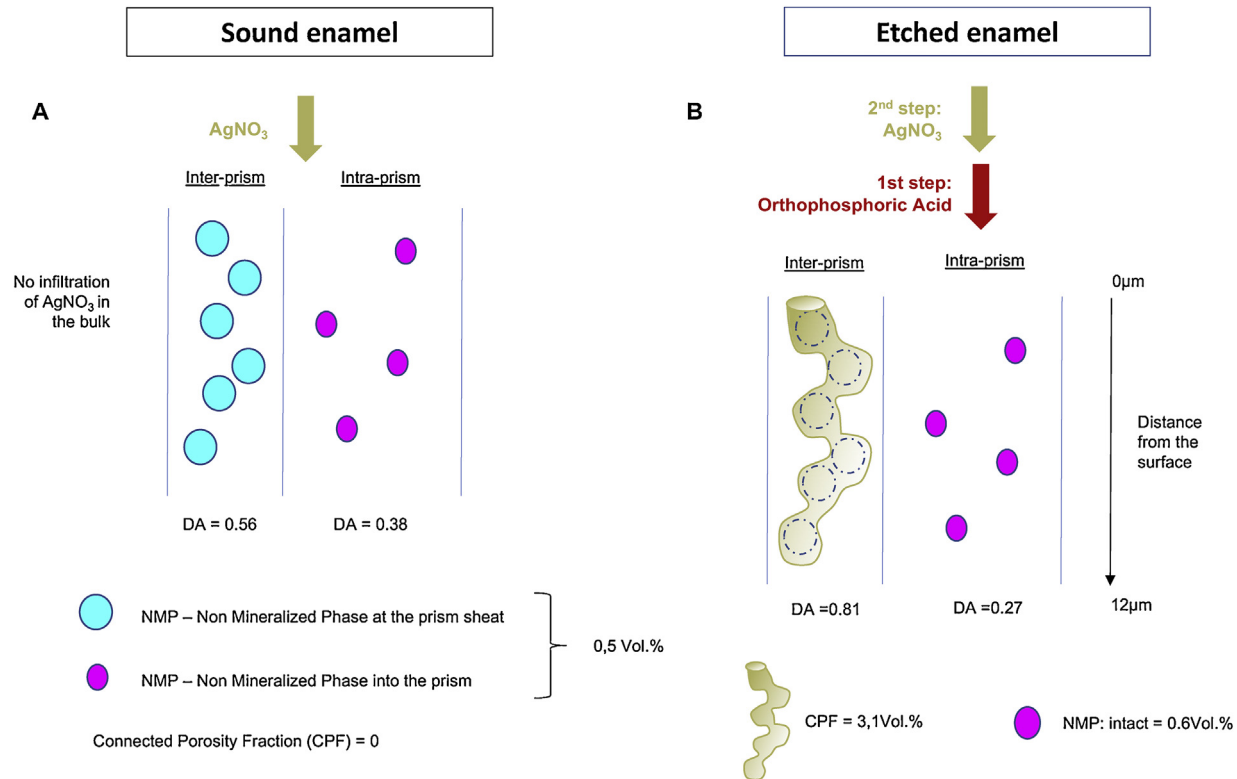


Fig. 6 – Schematic representation of the subsurface enamel acidic attack. (A) Healthy enamel showed a non mineralized phase which is a water and protein rich phase, having a content of 0.5 vol.%, with a bimodal distribution of non-mineralized regions, inside the prisms and between the prisms. No silver penetration was noticed in the healthy enamel, demonstrating the absence of open porosity. (B) After etching with an orthophosphoric acid, the silver nitrate penetrates and highlights a connected porosity fraction (CPF) mostly at the prism boundary. It decreases with depth. We see how these NMP are distributed along the prism C-axis: on SEM imaging, an area of black contrasts clearly defines the outline of the prisms (segmented and colored in cyan) while another population of black contrast is randomly distributed in the volume i.e. is located inside the prisms (colored in Magenta). The degree of anisotropy (DA) show how highly oriented substructures are within a volume. After acidic attack, the DA increases at the prism sheath. The NMP and the close hydroxyapatite are dissolved leading to a CPF of 3.1 vol.%.

decrease previously described [25,27,56,57]. The main features of the subsurface enamel acidic attack are illustrated in Fig. 6.

5. Conclusion

Beyond the enamel morphological characterization after acid etching, the quantitative 3D focused ion beam tomography led to the determination of three descriptors of the enamel evolution, i.e. NMP, DA and CPF. It could be helpful to widen this protocol to a larger set of teeth and patients and to study the different acidic degradation effects and the remineralization procedures effectiveness.

Acknowledgments

Thanks to Procter and Gamble company for financial support of FIB experiments. Thanks are also due to the CLYM (Centre Lyonnais de Microscopie) supported by the CNRS, the "GrandLyon" and the Rhône-Alpes Region for the access to the FIB/SEM device used in this study.

REFERENCES

- [1] Silverstone LM, Saxton CA, Dogon IL, Fejerskov O. Variation in the pattern of acid etching of human dental enamel examined by scanning electron microscopy. *Caries Res* 1975;9:373–87.
- [2] Carvalho TS, Colon P, Ganss C, Huysmans MC, Lussi A, Schlueter N, et al. Consensus report of the European Federation of Conservative Dentistry: erosive tooth wear—diagnosis and management. *Clin Oral Investig* 2015;19:1557–61.
- [3] Ganss C, Lussi A, Schlueter N. The histological features and physical properties of eroded dental hard tissues. *Monogr Oral Sci* 2014;25:99–107.
- [4] Shellis RP, Featherstone JDB, Lussi A. Understanding the chemistry of dental erosion. *Monogr Oral Sci* 2014;25:163–79.
- [5] Zentner A, Duschner H. Structural changes of acid etched enamel examined under confocal laser scanning microscope. *J Orofac Orthop* 1996;57:202–9.
- [6] Attin T, Wegehaupt FJ. Methods for assessment of dental erosion. *Monogr Oral Sci* 2014;25:123–42.
- [7] Paeppegaay A-M, Barker ML, Bartlett DW, Mistry M, West NX, Hellin N, et al. Measuring enamel erosion: a comparative

- study of contact profilometry, non-contact profilometry and confocal laser scanning microscopy. *Dent Mater* 2013;29:1265–72.
- [8] Narayan K, Subramaniam S. Focused ion beams in biology. *Nat Methods* 2015;12:1021–31.
- [9] Do T, Murphy G, Earl LA, Del Prete GQ, Grandinetti G, Li G-H, et al. Three-dimensional imaging of HIV-1 virological synapses reveals membrane architectures involved in virus transmission. *J Virol* 2014;88:10327–39.
- [10] Hayworth KJ, Xu CS, Lu Z, Knott GW, Fetter RD, Tapia JC, et al. Ultrastructurally smooth thick partitioning and volume stitching for large-scale connectomics. *Nat Methods* 2015;12:319–22.
- [11] Flori S, Jouneau P-H, Bailleul B, Gallet B, Estrozi LF, Moriscot C, et al. Plastid thylakoid architecture optimizes photosynthesis in diatoms. *Nat Commun* 2017;8:15885.
- [12] Narayan K, Danielson CM, Lagarec K, Lowekamp BC, Coffman P, Laquerre A, et al. Multi-resolution correlative focused ion beam scanning electron microscopy: applications to cell biology. *J Struct Biol* 2014;185:278–84.
- [13] Burnett TL, McDonald SA, Gholinia A, Geurts R, Janus M, Slater T, et al. Correlative tomography. *Sci Rep* 2014;4:4711.
- [14] Moroni R, Börner M, Zielke L, Schroeder M, Nowak S, Winter M, et al. Multi-scale correlative tomography of a Li-ion battery composite cathode. *Sci Rep* 2016;6:30109.
- [15] Cantoni M, Holzer L. Advances in 3D focused ion beam tomography. *MRS Bulletin* 2014;39:354–60.
- [16] Burnett TL, Kelley R, Winiarski B, Contreras L, Daly M, Gholinia A, et al. Large volume serial section tomography by Xe Plasma FIB dual beam microscopy. *Ultramicroscopy* 2016;161:119–29.
- [17] Viteau M, Reveillard M, Kime L, Rasser B, Sudraud P, Bruneau Y, et al. Ion microscopy based on laser-cooled cesium atoms. *Ultramicroscopy* 2016;164:70–7.
- [18] Parmenter Christopher, Baki Abdulraman, Shakesheff Kevin M. The application of cryogenic focused ion beam scanning electron microscopy to hydrogel characterization. *Microsc Microanal* 2016;22:192–3.
- [19] Schertel A, Snaidero N, Han H-M, Ruhwedel T, Laue M, Grabenbauer M, et al. Cryo FIB-SEM: volume imaging of cellular ultrastructure in native frozen specimens. *J Struct Biol* 2013;184:355–60.
- [20] Etiemble Aurélien, Tranchot Alix, Douillard Thierry, Idrissi Hassane, Maire Eric, Roué Lionel. Evolution of the 3D microstructure of a Si-based electrode for Li-ion batteries investigated by FIB/SEM tomography. *J Electrochem Soc* 2016;163:1550–9.
- [21] Besnard Nicolas, Etiemble Aurélien, Douillard Thierry, Dubrunfaut Olivier, Tran-Van Pierre, Gautier Laurent, et al. Multiscale morphological and electrical characterization of charge transport limitations to the power performance of positive electrode blends for lithium-ion batteries. *Adv Energy Mater* 2017;7:1602239.
- [22] Utke Ivo, Hoffmann Patrik, Melngailis John. Gas-assisted focused electron beam and ion beam processing and fabrication. *J Vac Sci Technol B* 2008;26:1197.
- [23] Shi C, Luu DK, Yang Q, Liu J, Chen J, Ru C, et al. Recent advances in nanorobotic manipulation inside scanning electron microscopes. *Microsyst Nanoeng* 2016;2:16024.
- [24] Wu Y-Q, Arsecularatne JA, Hoffman M. Effect of acidity upon attrition-corrosion of human dental enamel. *J Mech Behav Biomed Mater* 2015;44:23–34.
- [25] Zhang Y, Arsecularatne JA, Hoffman M. The effects of three different food acids on the attrition-corrosion wear of human dental enamel. *J Phys Appl Phys* 2015;48:285401.
- [26] Pecnik CM, Courty D, Muff D, Spolenak R. Fracture toughness of esthetic dental coating systems by nanoindentation and FIB sectional analysis. *J Mech Behav Biomed Mater* 2015;47:1–11.
- [27] Arsecularatne JA, Hoffman M. An in vitro study of the microstructure, composition and nanoindentation mechanical properties of remineralizing human dental enamel. *J Phys Appl Phys* 2014;47(31):315–403.
- [28] Bakhsh TA, Sadr A, Mandurah MM, Shimada Y, Zakaria O, Tagami J. In situ characterization of resin-dentin interfaces using conventional vs. cryofocused ion-beam milling. *Dent Mater* 2015;31:833–44.
- [29] Bakhsh TA. Ultrastructural features of dentinoenamel junction revealed by focused gallium ion beam milling. *J Microsc* 2016;264(1):14–21.
- [30] Marghalani Hanadi Yousif, Bakhsh Turki, Sadr Alireza, Tagami Junji. Ultra-structural characterization of enamel-resin interface using FIB-TEM technology. *J Adhes Sci Technol* 2014;28:1005–19.
- [31] Mukherjee K, Ruan Q, Liberman D, White SN, Moradian-Oldak J. Repairing human tooth enamel with leucine-rich amelogenin peptide-chitosan hydrogel. *J Mater Res* 2016;31:556–63.
- [32] Sebastiani M, Massimi F, Merlati G, Bemporad E. Residual micro-stress distributions in heat-pressed ceramic on zirconia and porcelain-fused to metal systems: analysis by FIB-DIC ring-core method and correlation with fracture toughness. *Dent Mater* 2015;31:1396–405.
- [33] Sui T, Lunt AJG, Baimpas N, Sandholzer MA, Li T, Zeng K, et al. Understanding nature's residual strain engineering at the human dentine-enamel junction interface. *Acta Biomater* 2016;32:256–63.
- [34] Chan YL, Ngan AHW, King NM. Use of focused ion beam milling for investigating the mechanical properties of biological tissues: a study of human primary molars. *J Mech Behav Biomed Mater* 2009;2:375–83.
- [35] Camposilvan Erik, Anglada Marc. Micropillar compression inside zirconia degraded layer. *J Eur Ceram Soc* 2015;35:4051–8.
- [36] Mainjot AK, Douillard T, Gremillard L, Sadoun MJ, Chevalier J. 3D-characterization of the veneer-zirconia interface using FIB nano-tomography. *Dent Mater* 2013;29:157–65.
- [37] Rueda AO, Seuba J, Anglada M, Jiménez-Piqué E. Tomography of indentation cracks in feldspathic dental porcelain on zirconia. *Dent Mater* 2013;29:348–56.
- [38] Jiménez-Piqué E, Ramos A, Muñoz-Tabares JA, Hatton A, Soldera F, Mücklich F, et al. Focused ion beam tomography of zirconia degraded under hydrothermal conditions. *J Eur Ceram Soc* 2012;32:2129–36.
- [39] Gremillard L, Chevalier J, Martin L, Douillard T, Begand S, Hans K, et al. Sub-surface assessment of hydrothermal ageing in zirconia-containing femoral heads for hip joint applications. *Acta Biomater* 2018;68:286–95.
- [40] Sanon C, Chevalier J, Douillard T, Kohal RJ, Coelho PG, Hjerpe J, et al. Low temperature degradation and reliability of one-piece ceramic oral implants with a porous surface. *Dent Mater* 2013;29:389–97.
- [41] Earl JS, Leary RK, Perrin JS, Brydson R, Harrington JP, Markowitz K, et al. Characterization of dentine structure in three dimensions using FIB-SEM. *J Microsc* 2010;240:1–5.
- [42] Sezen M, Sadighikia S. 3D electron microscopy investigations of human dentin at the micro/nano-scale using focused ion beam based nanostructuring. *RSC Adv* 2014;5:7196–9.
- [43] Coutinho E, Cardoso MV, Fernandes CP, Neves AA, Gouveia CVD, Landuyt KLV, et al. Nanoleakage distribution at adhesive-dentin interfaces in 3D. *J Dent Res* 2011;90:1019–25.
- [44] Odgaard A, Kabel J, van Rietbergen B, Dalstra M, Huiskes R. Fabric and elastic principal directions of cancellous bone are closely related. *J Biomech* 1997;30:487–95.

- [45] Musy SN, Maquer G, Panyasantisuk J, Wandel J, Zysset PK. Not only stiffness, but also yield strength of the trabecular structure determined by non-linear μ FE is best predicted by bone volume fraction and fabric tensor. *J Mech Behav Biomed Mater* 2017;65:808–13.
- [46] Odgaard A. Three-dimensional methods for quantification of cancellous bone architecture. *Bone* 1997;20:315–28.
- [47] Schindelin J, Arganda-Carreras I, Frise E, Kaynig V, Longair M, Pietzsch T, et al. Fiji: an open-source platform for biological-image analysis. *Nat Methods* 2012;9:676–82.
- [48] Sonka M, Hlavac V, Boyle R. Image processing, analysis, and machine vision. Cengage Learning; 2014.
- [49] Fehrenbach J, Weiss P, Lorenzo C. Variational algorithms to remove stationary noise: applications to microscopy imaging. *IEEE Trans Image Process Publ IEEE Signal Process Soc* 2012;21:4420–30.
- [50] Bolte S, Cordelières FP. A guided tour into subcellular colocalization analysis in light microscopy. *J Microsc* 2006;224:213–32.
- [51] Doube M, Kłosowski MM, Arganda-Carreras I, Cordelières FP, Dougherty RP, Jackson JS, et al. BoneJ: free and extensible bone image analysis in ImageJ. *Bone* 2010;47:1076–9.
- [52] Harrigan TP, Mann RW. Characterization of microstructural anisotropy in orthotropic materials using a second rank tensor. *J Mater Sci* 1984;19:761–7.
- [53] Xie Z, Kilpatrick NM, Swain MV, Munroe PR, Hoffman M. Transmission electron microscope characterisation of molar-incisor-hypomineralisation. *J Mater Sci Mater Med* 2008;19:3187–92.
- [54] Lussi A, Schlueter N, Rakhamatullina E, Ganss C. Dental erosion—an overview with emphasis on chemical and histopathological aspects. *Caries Res* 2011;45(Suppl. 1):2–12.
- [55] Xue J, Li W, Swain MV. In vitro demineralization of human enamel natural and abraded surfaces: a micromechanical and SEM investigation. *J Dent* 2009;37:264–72.
- [56] Elfallah HM, Bertassoni LE, Charadram N, Rathsam C, Swain MV. Effect of tooth bleaching agents on protein content and mechanical properties of dental enamel. *Acta Biomater* 2015;20:120–8.
- [57] Yahyazadehfar M, Arola D. The role of organic proteins on the crack growth resistance of human enamel. *Acta Biomater* 2015;19:33–45.